



Oxidative dehydrogenation and dry reforming of *n*-butane with CO₂ over NiFe bimetallic catalysts

Xiaodan Li^{a,b}, Binhang Yan^{a,c}, Siyu Yao^c, Shyam Kattel^c, Jingguang G. Chen^{b,c,*}, Tiefeng Wang^{a,**}

^a Beijing Key Laboratory of Green Reaction Engineering and Technology, Department of Chemical Engineering, Tsinghua University, Beijing 100084, China

^b Department of Chemical Engineering, Columbia University, New York, NY 10027, USA

^c Chemistry Department, Brookhaven National Laboratory, New York, NY 11973, USA

ARTICLE INFO

Keywords:

Oxidative dehydrogenation
Dry reforming
n-Butane
1,3-Butadiene
CO₂
Syngas
NiFe bimetallic catalysts

ABSTRACT

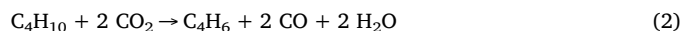
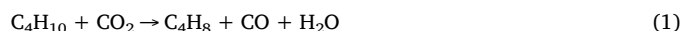
The oxidative dehydrogenation of *n*-butane to 1,3-butadiene using CO₂ as a soft oxidant is investigated over oxide-supported NiFe bimetallic catalysts. Dry reforming of *n*-butane with CO₂ to syngas is also studied under identical conditions for comparison. The Ni₁Fe₃/CeO₂ catalyst is identified as a promising catalyst for the oxidative dehydrogenation to 1,3-butadiene via the C–H bond cleavage, while the Ni₃Fe₁/CeO₂ catalyst mainly promotes the dry reforming pathway via the C–C bond scission. The oxidation states of Ni and Fe are determined by X-ray absorption fine structure (XAFS) measurements under reaction conditions. Density functional theory (DFT) calculations are performed to further understand the different reaction pathways. Furthermore, the effect of oxide supports is studied for the Ni₁Fe₃ bimetallic catalysts, showing that highly reducible supports, CeO₂ and CeO₂-ZrO₂, promote the production of 1,3-butadiene, whereas the ZrO₂ support significantly suppresses the oxidative dehydrogenation.

1. Introduction

As an important intermediate for the petrochemical industry [1,2], 1,3-butadiene can be widely used to make synthetic rubbers, plastics, resins, automotive fuels and other valuable products [3,4]. Over the past decade, the on-purpose production of 1,3-butadiene from butanes is developed as a promising alternative for its conventional supply from naphtha cracking [4–6]. The non-oxidative dehydrogenation of *n*-butane is a highly endothermic process that requires high operating temperatures to obtain a sufficient conversion, leading to thermal cracking and catalyst deactivation due to coke formation [2,5,7]. On the other hand, the oxidative dehydrogenation (ODH) of *n*-butane with oxygen is thermodynamically favorable and can be carried out at relatively low temperatures [8–10]. However, using oxygen as the oxidant has the issue of deep oxidation, where the dehydrogenated products would react rapidly with oxygen to form CO₂ and water, significantly decreasing the selectivities to 1,3-butadiene and butenes [6,8,10]. In this context, the use of soft oxidants, such as CO₂, for the ODH reaction offers an attractive alternative route for the selective dehydrogenation of butanes.

The prime greenhouse gas, CO₂, has been reported as a soft oxidant for ODH of light alkanes to their respective alkenes [11–13]. Using CO₂

in a catalytic process to produce valuable chemicals is an important strategy to migrate potential problems caused by CO₂ emission such as global climate change and ocean acidification [14,15]. Compared to ODH with oxygen, the use of CO₂ as a soft oxidant has the advantages to overcome deep oxidation reactions, consume rather than generate greenhouse gases, and reduce explosion risks from the dangerous mixture of oxygen and paraffin [11,12,16]. Furthermore, the unreacted CO₂ in excess can reduce coke formation at reaction temperatures via the reverse Boudouard reaction (CO₂ + C → 2 CO), thus increasing the catalyst stability [17,18]. In addition to ODH, another important pathway for converting *n*-butane in the presence of CO₂ is dry reforming to produce syngas, which can be subsequently transformed to value-added products by Fischer-Tropsch or methanol synthesis reactions [1,19–21]. The two important reaction pathways for *n*-butane conversion with CO₂, namely the ODH to 1,3-butadiene and butenes and the DRB to syngas, are described in the following equations:



The ODH of *n*-butane with CO₂ is proposed to occur through a Mars-

* Corresponding author at: Department of Chemical Engineering, Columbia University, New York, NY 10027, USA.

** Corresponding author.

E-mail addresses: jgchen@columbia.edu (J.G. Chen), wangtf@tsinghua.edu.cn (T. Wang).

van-Krevelentype (MVK) mechanism, where the catalyst first dehydrogenates *n*-butane into C₄ alkenes and H₂, and then H₂ reduces CO₂ to CO through the reverse water-gas shift reaction (RWSR), producing H₂O as a byproduct [22,23]. Although a large number of mixed metal oxides and supported metal catalysts are extensively investigated for the ODH of *n*-butane with oxygen, very few catalysts have been tested for the ODH of *n*-butane where CO₂ is used as an oxidant. Several recent publications reported the ODH of *n*-butane with CO₂ over titanium pyrophosphates and vanadium-based catalysts, but they mainly focused on the production of butenes instead of 1,3-butadiene [22,24–26]. Besides, the titanium pyrophosphates and vanadium-based catalysts showed problems of fast deactivation and toxicity, respectively [26,27]. Dasireddy et al. [28] studied the effect of O₂, CO₂ and N₂O on Ni-Mo/Al₂O₃ catalyst for the ODH of *n*-butane. However, when CO₂ was used as the oxidant, the yield of 1,3-butadiene was limited by a low *n*-butane conversion (< 10%). Therefore, it is highly desirable to develop an efficient catalyst with enhanced stability for the ODH of *n*-butane with CO₂. In addition, the ODH reaction is supposed to occur simultaneously with the DRB reaction in the presence of CO₂, thus identifying highly selective catalysts is necessary to differentiate the two reaction pathways.

Previous studies show that Ni-based catalysts are potential options for various reactions requiring the activation of hydrocarbons (e.g., hydrogenation, dehydrogenation and dry reforming), owing to its availability, low cost and high activity for the cleavage of both C–C and C–H bonds [29]. However, Ni-based catalysts usually suffer from rapid deactivation and show a relatively low selectivity toward partial oxidation or reduction reactions. The modification of Ni with Fe is considered to be an effective way to tune reaction pathways and also to improve catalytic performances in terms of activity, selectivity and/or stability, which is usually dependent on the additive amount of Fe [30–32]. According to the MVK mechanism, the activation of CO₂ is also a critical step in improving the overall reaction activity [11]. It is generally believed that the activation of CO₂ occurs at the support or the interfacial sites between the active metal and the oxide support [33]. Therefore, the reducibility of metal oxide supports is a key factor. Reducible CeO₂ oxide should help accommodate CO₂ dissociation by cycling between oxidized Ce⁴⁺ and reduced Ce³⁺ states [20,34]. The combination of bimetallic active sites (i.e., Ni and Fe) over highly reducible metal oxide supports should increase the catalyst activity, selectivity and coke resistance.

This work reports the ODH and DRB of *n*-butane with CO₂ over NiFe bimetallic catalysts. Reactions were carried out over NiFe bimetallic catalysts with different Ni/Fe ratios as well as Ni and Fe monometallic catalysts to identify effective catalysts for both the ODH pathway to 1,3-butadiene using CO₂ as a soft oxidant and the DRB pathway to syngas. Multiple characterization measurements including X-ray diffraction (XRD), X-ray absorption fine structure (XAFS), chemisorption and temperature-programmed reduction (TPR) were used to reveal the structures and properties of supported NiFe catalysts. Density functional theory (DFT) calculations were performed to further compare the ODH and DRB pathways. The effect of CO₂/*n*-butane ratios on the overall reaction conversion and product distributions was also included. Finally, the support effect was investigated on CeO₂, ZrO₂ and CeO₂-ZrO₂ to compare catalyst activity, selectivity and stability.

2. Experimental

2.1. Catalyst preparation

The supported NiFe bimetallic catalysts were synthesized over three commercial supports including CeO₂ (35–45 m²/g, nanopowder, Sigma–Aldrich), ZrO₂ (80–120 m²/g, Alfa Aesar) and CeO₂-ZrO₂ (60–90 m²/g, nanopowder, Sigma–Aldrich). The incipient wetness co-impregnation method was adopted to maximize the NiFe bimetallic bond formation, as described previously [35]. Typically, the required

amounts of metal precursors, Ni(NO₃)₂·6H₂O and Fe(NO₃)₃·9H₂O (Alfa Aesar), were dissolved in an amount of distilled water just sufficient to fill the pores of the support. The precursor solution was then dropwise added to the support and was mixed thoroughly between droplets. After impregnation, the catalysts were dried at 353 K for 12 h, then ramped to 563 K with a heating rate of 0.8 K/min and calcined in air for 2 h. Metal loadings of the NiFe bimetallic catalysts were 1.5 wt%Ni–0.5 wt%Fe and 0.5 wt%Ni–1.5 wt%Fe, corresponding to a Ni:Fe atomic ratio of 3:1 and 1:3, respectively. The as-prepared Ni₁Fe₃/CeO₂ and Ni₁Fe₃/ZrO₂ catalysts were mechanically mixed with a weight ratio of 1:1 to obtain the physical mixture referred as Ni₁Fe₃/CeO₂ + Ni₁Fe₃/ZrO₂ to compare with the Ni₁Fe₃/CeO₂-ZrO₂ catalyst. The Ni₄/CeO₂ and Fe₄/CeO₂ monometallic catalysts with a metal loading of 2 wt% were also prepared by incipient wetness impregnation to serve as control samples to study the synergetic effect between Ni and Fe.

2.2. Catalyst characterization

Ex-situ synchrotron XRD measurements of fresh and spent catalysts were performed on the 17-BM beamline of Advanced Photon Source (APS) at Argonne National Lab (ANL) with a X-ray wavelength of 0.24182 Å [20]. The in-situ XAFS spectra of Ni and Fe K-edges were collected at the 2-2 beamline of the Stanford Synchrotron Radiation Lightsources (SSRL). The detailed procedures for sample preparation and data collection have been previously reported [36]. For each measurement, 50 mg of fresh catalyst (60–80 mesh) was loaded into a glassy-carbon tube (0.3 mm OD) with quartz wool packed at both sides of the sample. The sample was first reduced under a 50% H₂/He flow (10 ml/min) at 723 K for 1 h, and then the spectra were collected with the sample cooled down to 373 K in 50% H₂/He. Afterwards, the gas flow was switched to a mixture of reactants consisting of CO₂ (4 ml/min), *n*-butane (2 ml/min) and He (4 ml/min). Then the sample was heated to 873 K with a ramp of 21 K/min. After 85 min of reaction, the sample was cooled down to 373 K under the reactant flow to take the XAFS spectra.

Pulse CO chemisorption was carried out in an Altamira AMI-300-*ip* instrument to estimate the number of metal active sites for the supported catalysts. For each test, approximately 100 mg of fresh catalyst was loaded into a U-shaped quartz tube and dried in He (30 ml/min) at 393 K for 30 min. The sample was reduced in 10% H₂/Ar (30 ml/min) with a heating rate of 10 K/min from 323 K to 723 K and held at 723 K for 45 min. The reduced catalyst was then purged with pure He (50 ml/min) at 723 K for 20 min to remove the absorbed H₂ on the catalyst surface and cooled down to 313 K. Subsequently, pulses of 10% CO in He (590 μL loop) were consecutively injected into the He stream until the effluent peak area of the pulses became constant. The amount of CO flowing out of the quartz tube was measured with a thermal conductivity detector (TCD). The CO uptake results provided a means to compare the number of metal active sites among the various supported catalysts.

TPR experiments were performed in the same Altamira AMI-300-*ip* apparatus. For each TPR experiment, approximately 50 mg of fresh catalyst, loaded into a U-shaped quartz tube, was first pretreated with 10% O₂/He (30 ml/min) at 723 K for 1 h and then cooled to 323 K in pure He. The flow was then switched to 10% H₂/Ar with a constant flow rate of 30 ml/min, and the TPR measurement was carried out with a heating rate of 10 K/min to 973 K. The H₂ consumption as a function of reduction temperature was recorded by TCD, which can be used to compare the reducibility of supported metals.

The temperature programmed oxidation-thermogravimetric analysis (TPO-TGA) technique was employed to analyze the carbon deposits on spent catalysts. The TGA analyses were performed using a Pyris Series-Diamond TG/DTA instrument with a precision of temperature measurement of ± 0.1 K and an accuracy of weight measurement of 0.01%. Approximately 30 mg of the spent catalyst was loaded and pretreated in Ar (30 ml/min) at 473 K for 70 min. The

sample was weighed again and then heated with a ramp of 10 K/min from 473 K to 1273 K in air (100 ml/min). The loss of catalyst weight as a function of temperature was recorded to estimate the amount of deposited carbon.

2.3. Flow reactor studies

Reactions of *n*-butane and CO₂ over supported catalysts were performed in a quartz tube reactor (4.0 mm ID) under atmospheric pressure. In a typical experiment, 100 mg of fresh catalyst sieved to 40–60 mesh was mixed with 400 mg of acid-purified quartz that was pre-calcined at 1173 K in air for 2 h and sieved to 40–60 mesh. This mixture of catalyst and inert diluent was loaded into the isothermal region of the reactor. The catalyst was in-situ reduced in 50% H₂/Ar (40 ml/min) at 723 K for 1 h prior to reaction. Then *n*-butane, CO₂ and Ar as a diluent were introduced into the reactor at a ratio of 1:2:17 with a constant total flow rate of 40 ml/min. For steady-state measurements, the reaction system was heated to 873 K and kept at this temperature for over 8 h. The gas products were sampled and analyzed online using a gas chromatography (Agilent 7890 B), which was equipped with two GC columns (HP-PLOT-Q 30 m × 0.53 mm × 40 μm and HP-Mole-sieve 30 m × 0.53 mm × 25 μm, Agilent), a flame ionization detector (FID) and a TCD. Control experiments were carried out at 873 K using a blank quartz tube with and without the pretreated supports mixed with acid-purified quartz. Both cases showed little activity, indicating that the gas-phase reaction, acid-purified quartz and bare supports have negligible effect on the reaction.

The conversions of *n*-butane and CO₂, turnover frequencies (TOF) based on *n*-butane and CO₂, and selectivity and yield of products at the steady-state, are defined as follows:

$$X_{\text{CO}_2} = \frac{n_{\text{CO}_2}^{\text{inlet}} - n_{\text{CO}_2}^{\text{outlet}}}{n_{\text{CO}_2}^{\text{inlet}}} \times 100\% \quad (4)$$

$$X_{n\text{-C}_4\text{H}_{10}} = \frac{n_{n\text{-C}_4\text{H}_{10}}^{\text{inlet}} - n_{n\text{-C}_4\text{H}_{10}}^{\text{outlet}}}{n_{n\text{-C}_4\text{H}_{10}}^{\text{inlet}}} \times 100\% \quad (5)$$

$$\text{TOF}_{\text{CO}_2} = \frac{X_{\text{CO}_2} \times F_{\text{CO}_2}^{\text{inlet}} \times P^{\text{inlet}}}{U_{\text{CO-uptake}} \times m_{\text{catalyst}} \times T^{\text{inlet}} \times R} \quad (\text{min}^{-1}) \quad (6)$$

$$\text{TOF}_{n\text{-C}_4\text{H}_{10}} = \frac{X_{n\text{-C}_4\text{H}_{10}} \times F_{n\text{-C}_4\text{H}_{10}}^{\text{inlet}} \times P^{\text{inlet}}}{U_{\text{CO-uptake}} \times m_{\text{catalyst}} \times T^{\text{inlet}} \times R} \quad (\text{min}^{-1}) \quad (7)$$

$$S_{\text{product } i} = \frac{n_{\text{product } i}^{\text{outlet}}}{n_{n\text{-C}_4\text{H}_{10}}^{\text{inlet}} - n_{n\text{-C}_4\text{H}_{10}}^{\text{outlet}}} \times 100\% \quad (8)$$

$$Y_{\text{product } i} = \frac{n_{\text{product } i}^{\text{outlet}}}{n_{n\text{-C}_4\text{H}_{10}}^{\text{inlet}}} \times 100\% \quad (9)$$

where X_{CO_2} and $X_{n\text{-C}_4\text{H}_{10}}$ are *n*-butane, respectively; $n_{\text{CO}_2}^{\text{inlet}}$ and $n_{n\text{-C}_4\text{H}_{10}}^{\text{inlet}}$ are *n*-butane (mol/min) at the inlet, respectively; $n_{\text{CO}_2}^{\text{outlet}}$, $n_{n\text{-C}_4\text{H}_{10}}^{\text{outlet}}$ and $n_{\text{product } i}^{\text{outlet}}$ are *n*-butane and products (mol/min) at the outlet, respectively; $F_{\text{CO}_2}^{\text{inlet}}$ and $F_{n\text{-C}_4\text{H}_{10}}^{\text{inlet}}$ are *n*-butane (m³/min) at the inlet, respectively; T^{inlet} is J/(K mol).

2.4. DFT calculations

Spin-polarized DFT [37,38] calculations were performed using the Vienna Ab-Initio Simulation Package (VASP) code [39,40]. Projector augmented wave potentials were used to describe the core electrons with the generalized gradient approximation (GGA) [41,42] using PW91 functionals [43]. The Kohn-Sham one-electron wave functions were expanded by using a plane wave basis set with a kinetic energy cutoff of 400 eV. The Ni(111) surface was modeled using a four layer 5 × 5 surface slab. The FeO/Ni(111) interface was modeled by depositing a small Fe₆O₉ cluster on a three layer 7 × 7 Ni(111) surface. The

Brillouin zone was sampled using a 3 × 3 × 1 k-point grid in the Monkhorst-Pack [44] scheme and a Γ -point on Ni(111) and FeO/Ni(111), respectively. A 14 Å thick vacuum was added along the direction perpendicular to the surface in the initial slab model to avoid the artificial interactions between the slab and its periodic images. During geometry optimization, the atoms in the top two layers were allowed to relax while the atoms in the rest layers were fixed. Ionic positions were optimized until the Hellman-Feynman force on each ion was smaller than 0.02 eV/Å. The binding energy (BE) of an adsorbate is calculated as:

$$\text{BE}(\text{adsorbate}) = E(\text{slab} + \text{adsorbate}) - E(\text{slab}) - E(\text{adsorbate}) \quad (10)$$

where $E(\text{slab} + \text{adsorbate})$, $E(\text{slab})$ and $E(\text{adsorbate})$ are the total energies of slab with adsorbate, clean slab and adsorbate species in gas phase, respectively.

3. Results

3.1. Thermodynamic analysis

Thermodynamic analysis for the reactions of *n*-butane and CO₂ was performed using the commercial HSC Chemistry 8 software based on the Gibbs free energy minimization algorithm. The equilibrium compositions for both the ODH and DRB reactions were calculated from 373 K to 1173 K at 1 atm with different inlet feed ratios of CO₂/*n*-butane, providing insights into the effects of variables and thermodynamic limitations. As shown in Fig. 1, both the ODH and DRB reactions are highly endothermic at low temperatures due to the stable nature of reactants. Fig. 1(a), (d) and (g) display the equilibrium plots for DRB of *n*-butane to CO, H₂ and H₂O via RWSR. Regardless of the CO₂/*n*-butane feed ratios, the production of H₂ and CO starts to progressively increase at 473 K and the H₂/CO ratio reaches 0.625 at 853 K, consistent with the stoichiometric coefficients of DRB as Eq. (3). At temperatures above 853 K, CO₂ is completely consumed and *n*-butane conversions are 0.25, 0.5 and 1.0 at the CO₂/*n*-butane feed ratios of 1.0, 2.0 and 4.0, respectively. The equilibrium compositions for the ODH of *n*-butane to butenes and 1,3-butadiene along with the CO and H₂O byproducts are presented in Fig. 1(b), (e) and (h). The formation of butenes is observed above 473 K, while 1,3-butadiene is produced at 773 K or higher. When CO₂ and *n*-butane are set at a feed ratio of 1:1, butenes are the main products with only a small amount of 1,3-butadiene generated at higher temperatures. When CO₂ and *n*-butane are set at a feed ratio of 2:1 or 4:1, the equilibrium amount of butenes first increases then decreases, while the equilibrium amount of 1,3-butadiene increases progressively to become the main product. This trend fits the consecutive reaction pathway for converting *n*-butane to butenes and further to 1,3-butadiene. The CO and H₂O byproducts are generated with an equal molar ratio. The thermodynamic plots in Fig. 1(c), (f) and (i) include the components of *n*-butane, CO₂, butenes, 1,3-butadiene, CO, H₂ and H₂O with the assumption that both the ODH and DRB reactions are taking place concurrently. It clearly shows that the DRB pathway is more thermodynamically favorable than ODH under the same condition. Therefore, it is critical to identify catalysts that can kinetically promote the ODH pathway. The optimal feed ratio of CO₂/*n*-butane for producing 1,3-butadiene is suggested to be 2:1. The reaction temperature for evaluating supported catalysts at the steady-state is selected to be 873 K to obtain an appropriate activity of gas-phase reaction and also avoid rapid catalyst deactivation by sintering and coking.

3.2. Catalyst characterization

3.2.1. XRD

The XRD patterns of both fresh and spent catalysts are compared in Fig. 2 to reveal the structural properties of catalysts before and after reaction. As shown in Fig. 2(a), the characteristic peaks of Ni₁Fe₃/CeO₂

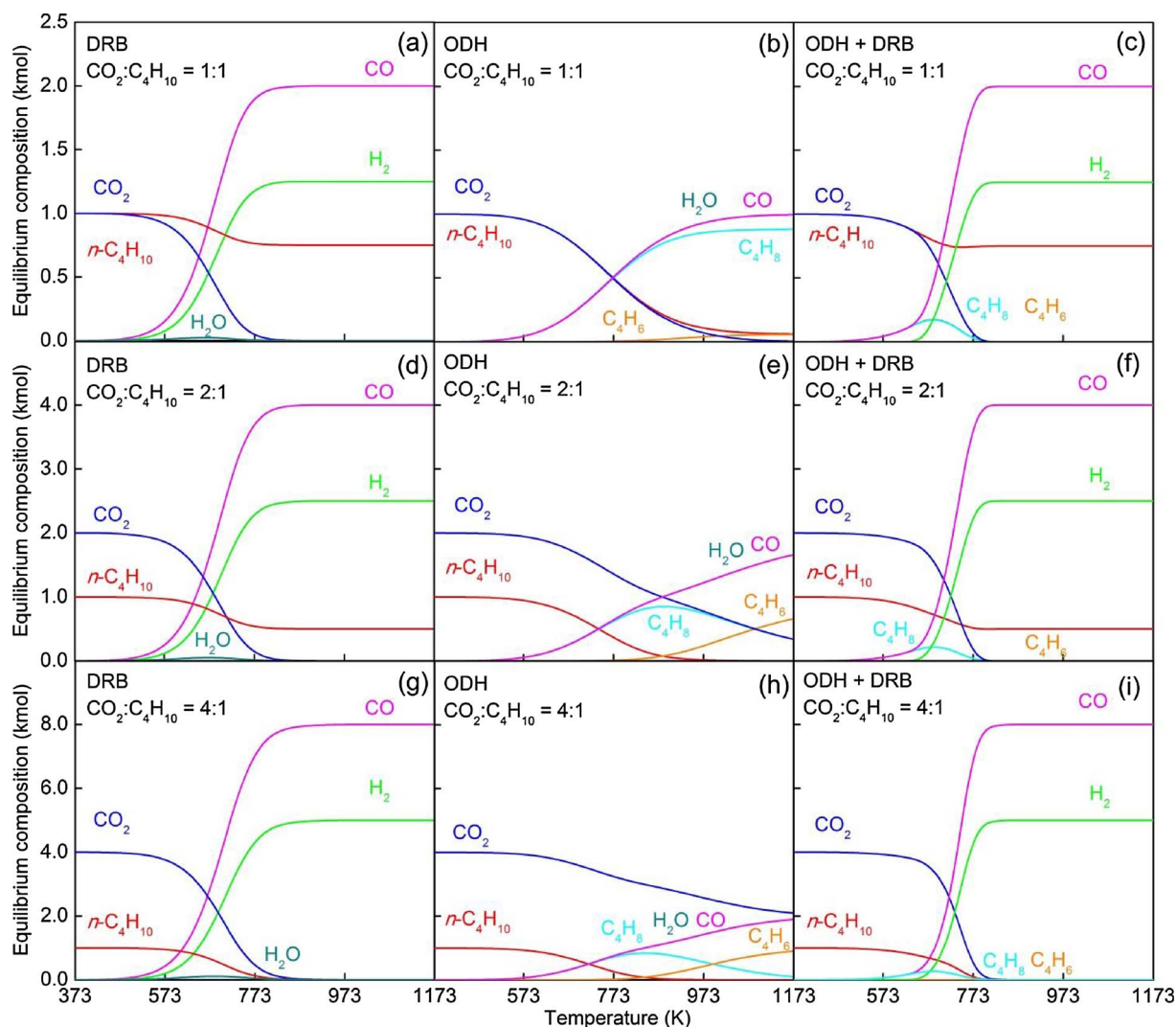


Fig. 1. Thermodynamic equilibrium plots for the reactions of *n*-butane and CO₂ at 1 atm from 373 to 1173 K (a) DRB at CO₂:C₄H₁₀ = 1:1, (b) ODH at CO₂:C₄H₁₀ = 1:1, (c) DRB and ODH at CO₂:C₄H₁₀ = 1:1, (d) DRB at CO₂:C₄H₁₀ = 2:1, (e) ODH at CO₂:C₄H₁₀ = 2:1, (f) DRB and ODH at CO₂:C₄H₁₀ = 2:1, (g) DRB at CO₂:C₄H₁₀ = 4:1, (h) ODH at CO₂:C₄H₁₀ = 4:1, and (i) DRB and ODH at CO₂:C₄H₁₀ = 4:1.

are observed at 4.42°, 5.11°, 7.24°, 8.47°, 8.85° and 10.23°, corresponding to the (111), (200), (220), (311), (222) and (400) planes of the fluorite structure of CeO₂, respectively [45]. For Ni₁Fe₃/ZrO₂, the feature peaks at 3.73°, 4.36°, 4.87°, 5.28°, 6.26° and 8.35° represent the monoclinic ZrO₂, while the peaks at 5.40°, 7.65° and 8.94° correspond to the tetragonal ZrO₂ [46]. Broad diffraction peaks of a cubic fluorite phase of Ce_{0.5}Zr_{0.5}O₂ are identified for Ni₁Fe₃/CeO₂-ZrO₂, indicating the incorporation of ZrO₂ into the CeO₂ lattice to form a solid solution [47]. The XRD pattern of physically mixed Ni₁Fe₃/CeO₂ + Ni₁Fe₃/ZrO₂ catalyst appears to be an overlap of those of Ni₁Fe₃/CeO₂ and Ni₁Fe₃/ZrO₂. For all four Ni₁Fe₃ catalysts, the crystalline structures of their supports (i.e., CeO₂, ZrO₂ and CeO₂-ZrO₂) are found to be stable after reaction, as shown by the nearly identical XRD patterns of the fresh and spent samples.

Fig. 2(b) shows the XRD patterns in the 2θ range of 5.4°–7.0° for the CeO₂ supported monometallic Ni, Fe and NiFe bimetallic catalysts. For the fresh samples, characteristic peaks of Ni oxides are not observed for all three Ni-containing catalysts, while two feature peaks at 5.71° and 6.61° assigned to the (311) and (400) reflections of α-Fe₂O₃ are found in the XRD spectra of Fe₄/CeO₂ and Ni₁Fe₃/CeO₂. The spent catalysts exhibit different XRD signatures compared to the fresh ones. The spent Ni₄/CeO₂ has the peak of Ni(111) plane at 6.80°. For Fe₄/CeO₂, the two characteristic peaks of α-Fe₂O₃ nearly disappear with the appearance of

a new peak at 5.45° corresponding to the (311) plane of Fe₃O₄, indicating the transformation of Fe species from Fe₂O₃ to Fe₃O₄. For the two NiFe bimetallic catalysts, Ni₁Fe₃/CeO₂ has the characteristic peak of Fe₃O₄ at 5.45°, while Ni₃Fe₁/CeO₂ exhibits the characteristic peak of Fe₂O₃ at 6.61°. Both bimetallic catalysts have an obvious feature peak at 6.75°, which is between the Fe₂O₃ and Ni(111) peaks. This peak is most likely derived from the Ni species, because a gradual shift of the peak position to a lower 2θ with a decreasing intensity is observed by comparing the Ni₄/CeO₂, Ni₃Fe₁/CeO₂ and Ni₁Fe₃/CeO₂ catalysts. The shift of this peak to a lower 2θ is probably due to the interaction between Ni and Fe.

3.2.2. CO chemisorption

In order to obtain a quantitative comparison of the number of metal active sites of different supported catalysts, CO uptake values are calculated according to CO chemisorption results with the assumption that each CO molecule corresponds to one active site. The results are shown in Table 1. Among the CeO₂ supported catalysts, the Ni₁Fe₃/CeO₂ and Ni₃Fe₁/CeO₂ bimetallic catalysts have higher CO uptake values than the corresponding monometallic catalysts, suggesting that the synergistic effect between Ni and Fe increases the CO binding sites of the catalysts. The CO uptake values of the Ni₁Fe₃ catalysts on different supports follow the trend of Ni₁Fe₃/CeO₂ > Ni₁Fe₃/ZrO₂ > Ni₁Fe₃/CeO₂-ZrO₂.

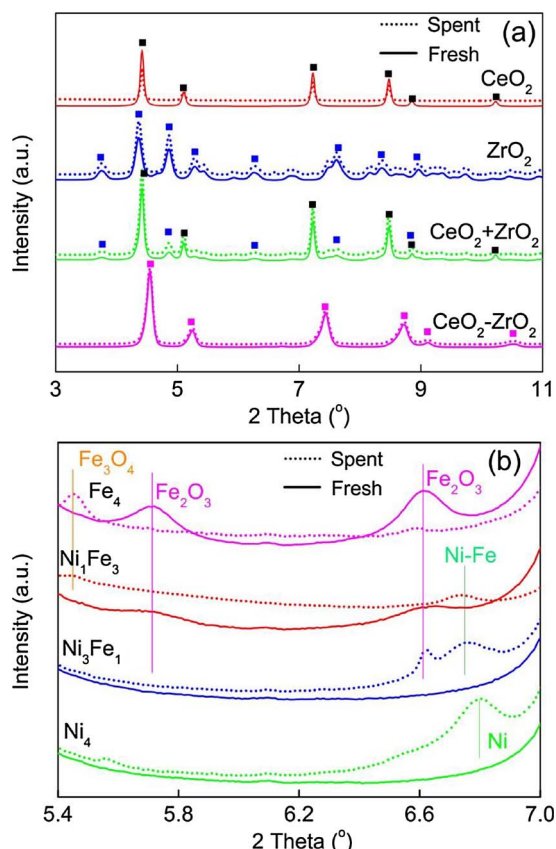


Fig. 2. XRD patterns of the fresh and spent catalysts: (a) Ni₁Fe₃ on different supports (3.0–11.0°) and (b) CeO₂ supported catalysts (5.4–7.0°).

3.2.3. TPR

Fig. 3 shows the H₂-TPR profiles of the CeO₂ supported NiFe bimetallic and the corresponding monometallic catalysts. Two reduction peaks at 500 K and 542 K are observed for Ni₄/CeO₂. The broad reduction peak at 542 K is assigned to the reduction of NiO particles, but the cause of appearing the sharp shoulder peak at 500 K remains controversial. Du et al. [48] suggested that the reduction peak in the low temperature range was probably due to the reduction of weakly interactive NiO species with CeO₂ supports, while Frusteri et al. [49] reported that the peak at 500 K was ascribed to the reduction of surface non-stoichiometric Ni³⁺ species such as NiO(OH). The profile of Fe₄/CeO₂ exhibits two reduction peaks at 596 K and 786 K, which are

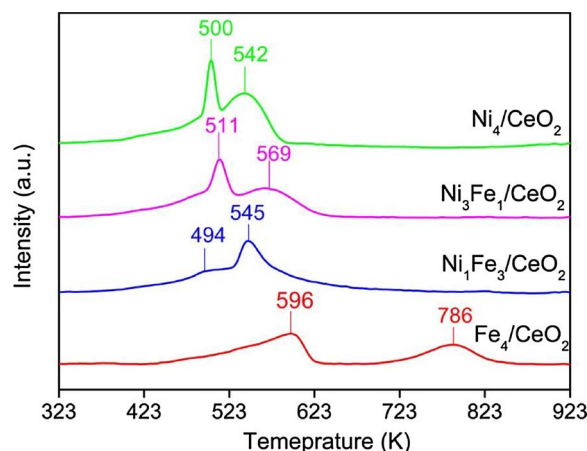


Fig. 3. TPR profiles of the CeO₂ supported NiFe bimetallic and the corresponding monometallic catalysts.

attributed to the reduction of Fe species, *i.e.*, Fe₂O₃ → Fe₃O₄ and Fe₃O₄ → Fe⁰, respectively [50]. It should be noted that if Fe species was totally reduced to Fe⁰, the reduction peak area for Fe₃O₄ → Fe⁰ should double that for Fe₂O₃ → Fe₃O₄. However, the two reduction peaks at 596 K and 786 K have similar areas, suggesting that the Fe species are not totally reduced to metallic state even after reduction at high temperatures. In the case of bimetallic catalysts, the Ni₃Fe₁/CeO₂ catalyst presents a very similar TPR profile as Ni₄/CeO₂, with the two reduction peaks slightly shifting to higher temperatures of 511 K and 569 K, showing that the modification of Ni with Fe leads to a decreased catalyst reducibility. However, the TPR profile of Ni₁Fe₃/CeO₂ exhibits a different trend, as its reduction peaks are much lower compared to Fe₄/CeO₂.

3.2.4. XAFS

As an important factor influencing the catalyst performance, the oxidation states of Ni and Fe heavily depend on the property of the support as well as the reaction conditions such as the reaction temperature and relative concentrations of CO₂ and H₂. In addition, the reducibility of the alkane itself can also affect the redox cycle of Fe species. *n*-Butane is more reducible than the well-studied methane and ethane. For the above reasons, it is worthwhile to confirm the oxidation states of Ni and Fe over the CeO₂ support under the specific conditions for the reaction of *n*-butane with CO₂. Therefore, the local environment of Ni and Fe species is investigated by in-situ XAFS analysis at the Ni and Fe K-edges for both Ni₃Fe₁/CeO₂ and Ni₁Fe₃/CeO₂. As shown in

Table 1
CO uptake values and flow reactor results.

Entry	Catalyst	CO uptake 10 ⁻⁶ mol/g	Conversion ^{a,b} (%)		TOF ^b (min ⁻¹)		Selectivity ^{b,c} (%)				Yield ^d (%)	
			CO ₂	<i>n</i> -C ₄ H ₁₀	CO ₂	<i>n</i> -C ₄ H ₁₀	C ₄ H ₆	C ₄ H ₈	CO	C ₁ -C ₃	ODH ^d	DRB ^d
1	Ni ₄ /CeO ₂	16.6	63.7	30.9	74.8	18.1	0.4	0	96.4	0.7	0.1	29.8
2 ^c	Ni ₄ /CeO ₂	–	25.3	10.2	71.5	17.1	0.9	0	96.9	1.7	0.1	9.9
3	Fe ₄ /CeO ₂	21.4	10.5	7.0	9.6	3.2	13.5	10	53.6	18.5	1.6	3.8
4	Ni ₁ Fe ₃ /CeO ₂	26.4	18.7	11.9	13.8	4.4	21.4	9.2	56.4	9.6	3.6	6.7
5	Ni ₃ Fe ₁ /CeO ₂	30.2	59.3	30.9	38.3	10.0	0.3	4.1	91.3	0.6	1.4	28.2
6 ^f	Ni ₃ Fe ₁ /CeO ₂	–	18.3	9.9	35.6	9.2	1.3	1.9	90.4	1.7	0.3	8.9
7	Ni ₁ Fe ₃ /ZrO ₂	21.2	35.1	15.8	32.3	7.3	3.7	5.2	85.7	5.3	1.4	13.5
8	Ni ₁ Fe ₃ /CeO ₂ -ZrO ₂	16.3	21.7	13.9	25.9	8.3	27.4	9.8	52.4	9.4	5.2	7.3
9	Ni ₁ Fe ₃ /CeO ₂ + Ni ₁ Fe ₃ /ZrO ₂	–	28.3	14.5	–	–	7.5	6.5	75.6	6.2	2.0	11.0

^a Reaction conditions: catalyst of 100 mg, 1 atm, 873 K, CO₂: *n*-butane: Ar = 2: 1: 17 with a total flow rate of 40 ml/min.

^b The conversions, TOFs and yields were calculated by averaging data points between 8–10 h at steady state.

^c C₄H₆, C₄H₈ and C₁-C₃ represent 1,3-butadiene, 1-butene and 2-butenes, and C₁-C₃ hydrocarbons including CH₄, C₂H₆, C₂H₄, C₃H₈ and C₃H₆, respectively.

^d Yield to ODH is the total yield of C₄H₆ and C₄H₈; yield to DRB is based on CO.

^e 35 mg of the Ni₄/CeO₂ catalyst was used to obtain an approximately 10% *n*-butane conversion.

^f 40 mg of the Ni₃Fe₁/CeO₂ catalyst was used to obtain an approximately 10% *n*-butane conversion.

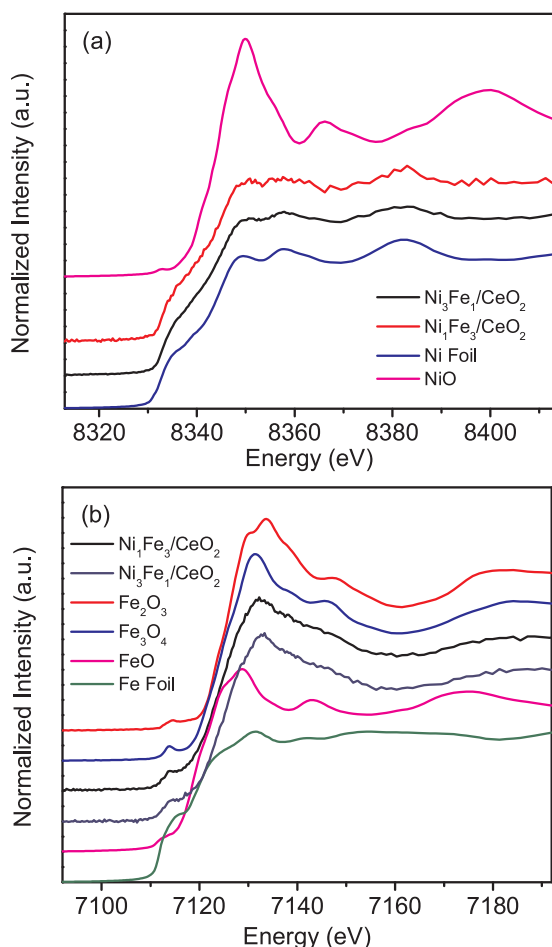


Fig. 4. Selected XANES profiles of $\text{Ni}_1\text{Fe}_3/\text{CeO}_2$ and $\text{Ni}_3\text{Fe}_1/\text{CeO}_2$ at (a) Ni and (b) Fe K-edges after reactions.

Table 2

Linear combination fitting results of NiFe/CeO_2 catalysts from XANES analysis.

Entry	Species (%)	Catalysts	
		$\text{Ni}_3\text{Fe}_1/\text{CeO}_2$	$\text{Ni}_1\text{Fe}_3/\text{CeO}_2$
1	Ni(0)	100	90.2
2	NiO	0	9.8
3	Fe(0)	32.5	19.3
4	FeO	0	7.4
5	Fe_3O_4	0	28.7
6	Fe_2O_3	67.5	44.6

Fig. 4(a) and (b), Ni species are mainly in the metallic state (0) while Fe species are in both metallic and oxidation states for both catalysts. The linear combination fitting results (Table 2) present that for $\text{Ni}_3\text{Fe}_1/\text{CeO}_2$, all the Ni species are reduced to Ni(0) while only one third of Fe species are reduced to Fe(0) and the rest of the Fe species remain as Fe_2O_3 . For $\text{Ni}_1\text{Fe}_3/\text{CeO}_2$, over 90% of Ni species are reduced to Ni(0) while Fe(0), FeO, Fe_3O_4 and Fe_2O_3 account for 19.3%, 7.4%, 28.7% and 44.6% of Fe species, respectively.

3.3. Catalytic evaluation

3.3.1. Bimetallic effect

The CeO_2 supported monometallic and bimetallic catalysts were evaluated in the gas-phase reactions of *n*-butane and CO_2 under the same conditions to investigate the bimetallic effect. The conversions of CO_2 and *n*-butane, and the selectivities to 1,3-butadiene and DRB are

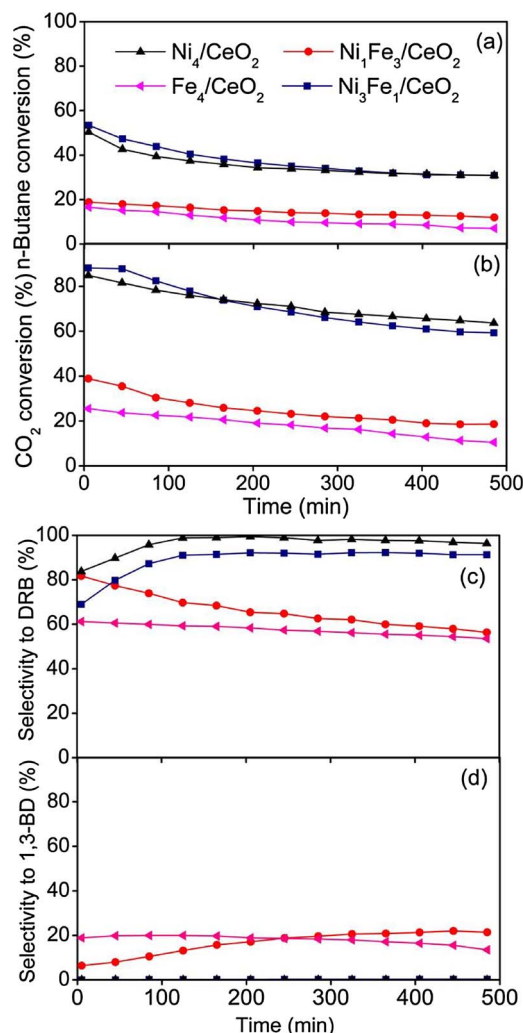


Fig. 5. Conversions of (a) CO_2 and (b) *n*-butane, and selectivities to (c) DRB and (d) 1,3-butadiene plotted versus reaction time over CeO_2 supported catalysts ($\text{CO}_2/\text{n-Butane}/\text{Ar} = 2:1:17$, 1 atm, 873 K).

plotted as a function of time on stream in Fig. 5. The average conversions, TOFs and product distributions at the steady-state are given in Table 1. Ni_4/CeO_2 is the most active and selective DRB catalyst, which exhibits the highest conversions of *n*-butane and CO_2 with over 96% of the products detected to be syngas. When Ni is modified by Fe to form $\text{Ni}_3\text{Fe}_1/\text{CeO}_2$, the bimetallic catalyst is still highly selective toward the DRB pathway with comparable conversions of *n*-butane and CO_2 . As shown in Fig. 5, the conversions of *n*-butane and CO_2 over both of the DRB catalysts gradually decrease with increasing reaction time due to catalyst deactivation, but the initial selectivity to DRB (based on CO) is much lower than its steady-state value, as the high catalyst activity at the beginning stage can lead to further conversion of CO to methane and also some cracking reactions to produce small hydrocarbon molecules (e.g., C_2H_4 , C_2H_6 , C_3H_6 and C_3H_8). Both Ni_4/CeO_2 and $\text{Ni}_3\text{Fe}_1/\text{CeO}_2$ have an approximately 4:1 ratio of TOF_{CO_2} versus $\text{TOF}_{\text{n-C}_4\text{H}_{10}}$.

The Fe_4/CeO_2 monometallic catalyst is much less active than Ni_4/CeO_2 , and the conversions of CO_2 and *n*-butane are 10.5% and 7.0%, respectively. However, a promising selectivity toward the ODH of *n*-butane is observed over Fe_4/CeO_2 , where 1,3-butadiene and butenes are generated with selectivities of 13.5% and 10.0%, respectively. In addition to ODH, DRB to syngas and crackings to $\text{C}_2\text{-C}_3$, especially ethylene, also occur over Fe_4/CeO_2 , accounting for 53.6% and 18.5% of the products, respectively. When Fe is modified with Ni to form $\text{Ni}_1\text{Fe}_3/\text{CeO}_2$, the conversions of CO_2 and *n*-butane increase to 18.7% and

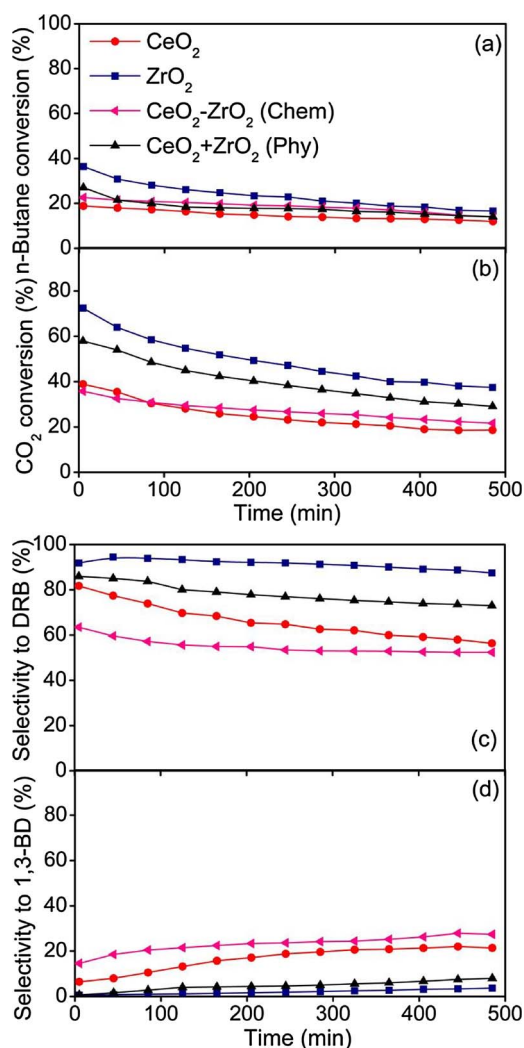


Fig. 6. Conversions of (a) CO_2 and (b) n -butane, and selectivities to (c) CO and (d) 1,3-butadiene plotted versus reaction time over supported Ni_1Fe_3 catalysts (CO_2/n -butane/Ar = 2:1:17, 1 atm, 873 K).

11.9%, respectively. Fig. 5(d) shows that although the selectivity to 1,3-butadiene over $\text{Ni}_1\text{Fe}_3/\text{CeO}_2$ is relatively low in the early stage of reaction, it increases gradually and finally approaches to 21.4% at steady-state. The $\text{Ni}_1\text{Fe}_3/\text{CeO}_2$ bimetallic catalyst is more active than the Fe_4/CeO_2 monometallic catalyst according to their TOFs. The ratio of TOF_{CO_2} versus $\text{TOF}_{n\text{-C}_4\text{H}_{10}}$ over $\text{Ni}_1\text{Fe}_3/\text{CeO}_2$ and Fe_4/CeO_2 is around 3:1, as the DRB and ODH reactions of n -butane with CO_2 occur simultaneously.

3.3.2. Support effect

Support effect on the extent of ODH versus DRB is investigated by comparing $\text{Ni}_1\text{Fe}_3/\text{CeO}_2$ with two other supported Ni_1Fe_3 catalysts, $\text{Ni}_1\text{Fe}_3/\text{ZrO}_2$ and $\text{Ni}_1\text{Fe}_3/\text{CeO}_2\text{-ZrO}_2$. The physically mixed catalyst $\text{Ni}_1\text{Fe}_3/\text{CeO}_2 + \text{Ni}_1\text{Fe}_3/\text{ZrO}_2$ is also evaluated for comparison. As shown in Fig. 6, the conversions of CO_2 and n -butane over all four catalysts progressively decrease during the reaction owing to different extents of catalyst deactivation. On the other hand, the selectivities to 1,3-butadiene and DRB gradually increase and decrease with the increasing reaction time, respectively. Compared with $\text{Ni}_1\text{Fe}_3/\text{CeO}_2$, $\text{Ni}_1\text{Fe}_3/\text{CeO}_2\text{-ZrO}_2$ appears to be a better catalyst with the highest selectivity of 27.4% to 1,3-butadiene at slightly higher conversions of CO_2 and n -butane. However, when ZrO_2 is used as the support, the Ni_1Fe_3 bimetallic catalyst becomes more selective toward dry reforming with a high selectivity over 85% to syngas, and it has a higher activity than $\text{Ni}_1\text{Fe}_3/\text{CeO}_2$ and $\text{Ni}_1\text{Fe}_3/\text{CeO}_2\text{-ZrO}_2$. Unlike using the $\text{CeO}_2\text{-ZrO}_2$ solid

solution as the support, the catalytic performance of the physically mixed catalyst $\text{Ni}_1\text{Fe}_3/\text{CeO}_2 + \text{Ni}_1\text{Fe}_3/\text{ZrO}_2$ is between those of $\text{Ni}_1\text{Fe}_3/\text{CeO}_2$ and $\text{Ni}_1\text{Fe}_3/\text{ZrO}_2$ without synergistic effects. The catalyst activities on the basis of steady-state conversions for the four Ni_1Fe_3 catalysts follow the trend of $\text{Ni}_1\text{Fe}_3/\text{ZrO}_2 > \text{Ni}_1\text{Fe}_3/\text{CeO}_2 + \text{Ni}_1\text{Fe}_3/\text{ZrO}_2 > \text{Ni}_1\text{Fe}_3/\text{CeO}_2\text{-ZrO}_2 > \text{Ni}_1\text{Fe}_3/\text{CeO}_2$. The ratio of ODH yield (i.e., total yield of 1,3-butadiene and butenes) versus DRB yield decreases in the order of $\text{Ni}_1\text{Fe}_3/\text{CeO}_2\text{-ZrO}_2 > \text{Ni}_1\text{Fe}_3/\text{CeO}_2 > \text{Ni}_1\text{Fe}_3/\text{CeO}_2 + \text{Ni}_1\text{Fe}_3/\text{ZrO}_2 > \text{Ni}_1\text{Fe}_3/\text{ZrO}_2$. The different product distributions of the Ni_1Fe_3 catalysts on different supports can be related to the differences of intrinsic properties of the supports, such as reducibility, oxygen mobility and carbon storage capacity, which will be discussed in detail in Section 4.

3.3.3. Catalyst deactivation

The studies of catalyst stability are very important for developing an efficient catalyst for the reactions of CO_2 and n -butane. The curves of the conversions of CO_2 and n -butane versus reaction time shown in Figs. 5 and 6 reveal that almost all the evaluated catalysts exhibit deactivation to some extent. For the CeO_2 supported catalysts, the stability of the bimetallic catalysts is enhanced compared to the corresponding monometallic catalysts. However, serious deactivation is observed over $\text{Ni}_1\text{Fe}_3/\text{ZrO}_2$. The $\text{Ni}_1\text{Fe}_3/\text{CeO}_2$ catalyst is more stable than the other catalysts, probably owing to the good carbon elimination ability of the CeO_2 support. Generally, catalyst deactivation is a complex phenomenon that has been attributed to the sintering or agglomeration of supported metals and the formation of coke. The comparison of XRD patterns between the spent and fresh catalysts in Section 3.1 indicates that there is no serious agglomeration of supported metals. Thus the catalyst deactivation is likely resulting from the formation of coke during the reaction.

The type and quantity of carbon deposits on the spent $\text{Ni}_1\text{Fe}_3/\text{CeO}_2$, $\text{Ni}_3\text{Fe}_1/\text{CeO}_2$, $\text{Ni}_1\text{Fe}_3/\text{ZrO}_2$ and $\text{Ni}_1\text{Fe}_3/\text{CeO}_2\text{-ZrO}_2$ catalysts are further analyzed by their TGA and derivative thermogravimetric (DTG) plots. Generally, the carbon species with a lower DTG peak temperature has a higher activity and can be easily removed and the peak area represents the amount of the corresponding carbon species. Fig. 7 shows that little carbon deposit is formed over $\text{Ni}_1\text{Fe}_3/\text{CeO}_2$ and $\text{Ni}_1\text{Fe}_3/\text{CeO}_2\text{-ZrO}_2$. However, when ZrO_2 is used as the support, a total carbon deposit of 5 wt% is observed, and two types of carbon deposits with nearly equal mass fraction can be identified by the two distinct peaks at 553 K and 643 K in the DTG plot of $\text{Ni}_1\text{Fe}_3/\text{ZrO}_2$. Compared with the Ni_1Fe_3 catalysts, the $\text{Ni}_3\text{Fe}_1/\text{CeO}_2$ catalyst is much less stable with a total carbon deposit of 10 wt%. Based on the DTG data shown in Fig. 7(b), there are three types of carbon deposits at 470 K, 553 K and 850 K with a mass fraction of 11.9%, 84.5% and 3.6%, respectively. The TGA analysis is consistent with the catalytic evaluation results. It is important to note that all the carbon deposits can be removed at the reaction temperature, i.e., 873 K, indicating an easy in-situ regeneration of the spent catalysts.

3.3.4. Effect of feed ratio of CO_2/n -butane

According to the thermodynamic analysis in Section 3.1, the ratio of ODH versus DRB as well as the product distribution of ODH reaction is predicted to be influenced by the feed ratio of CO_2/n -butane. Therefore, both ODH and DRB catalysts were evaluated using different inlet feed ratios of CO_2/n -butane. $\text{Ni}_3\text{Fe}_1/\text{CeO}_2$ and $\text{Ni}_1\text{Fe}_3/\text{CeO}_2$ were selected to be the representative of DRB and ODH catalysts, respectively, because both of them are CeO_2 supported Ni-Fe bimetallic catalysts and their only difference is the Ni/Fe ratio. As shown in Fig. 8(a), the conversion of n -butane over $\text{Ni}_1\text{Fe}_3/\text{CeO}_2$ gradually increases with an increasing inlet feed ratio of CO_2/n -butane. When the CO_2/n -butane ratio goes up to 4.0, the conversion of n -butane nearly doubles that at the ratio of 1.0. For the $\text{Ni}_3\text{Fe}_1/\text{CeO}_2$ catalyst, the inlet feed ratio of CO_2/n -butane shows a more significant effect on the conversion of n -butane, which increases from 30.9% to 70.9% when the CO_2/n -butane ratio increases from 2.0 to 4.0. Fig. 8(b) shows the correlation curves of product

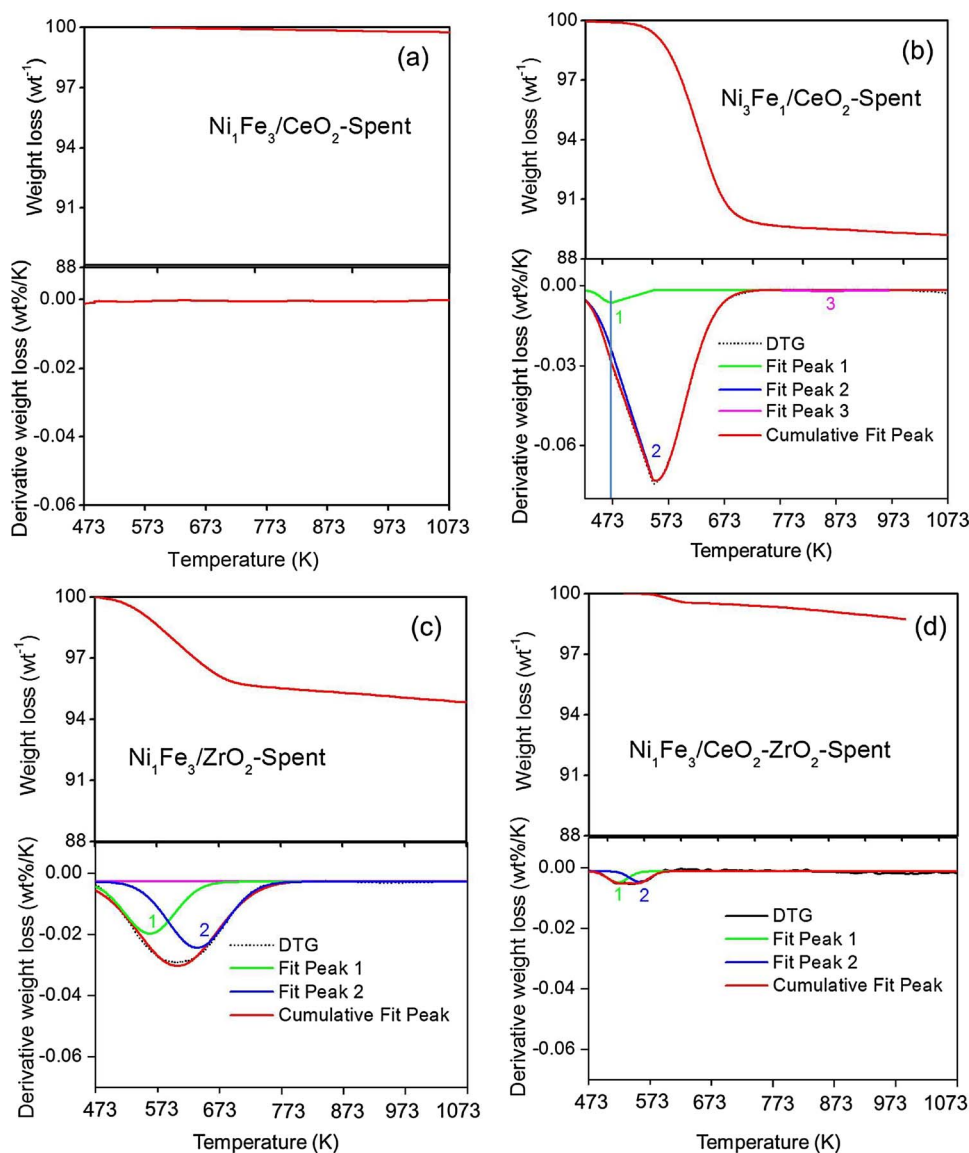


Fig. 7. TGA and DTG plots of the spent catalysts, (a) $\text{Ni}_1\text{Fe}_3/\text{CeO}_2$, (b) $\text{Ni}_3\text{Fe}_1/\text{CeO}_2$, (c) $\text{Ni}_1\text{Fe}_3/\text{ZrO}_2$ and (d) $\text{Ni}_1\text{Fe}_3/\text{CeO}_2\text{-ZrO}_2$.

selectivities with the inlet feed ratio of CO_2/n -butane. With an increasing CO_2/n -butane ratio, the selectivity to 1-butene and syngas linearly decreases and increases, respectively, while the selectivity to 1,3-butadiene first slightly increases and then decreases over $\text{Ni}_1\text{Fe}_3/\text{CeO}_2$. This experimental trend is consistent with the thermodynamic results that the extent of ODH *versus* DRB decreases by increasing the CO_2/n -butane ratio. For the $\text{Ni}_3\text{Fe}_1/\text{CeO}_2$ catalyst, an increase of the CO_2/n -butane ratio has very limited effect on the product distribution as CO remains to be the main product with a high selectivity over 90%.

4. Discussion

In the current study of n -butane with CO_2 , both the oxidative dehydrogenation and dry reforming reactions occur simultaneously, therefore it is very important to identify highly selective catalysts and differentiate the two reaction pathways. The results above demonstrate that reaction pathways of n -butane with CO_2 are significantly affected by the metal composition and support of catalysts. Fig. 9 further compares the catalyst activities and product distributions at the steady-state for all the studied catalysts, where the results were repeated for three times and presented with error bars. As shown in Fig. 9(a) and (b), Ni_4/CeO_2 and $\text{Ni}_3\text{Fe}_1/\text{CeO}_2$ with Ni as the dominating active metal are

identified as DRB catalysts with a selectivity of over 90% to syngas. For Fe_4/CeO_2 and $\text{Ni}_1\text{Fe}_3/\text{CeO}_2$ catalysts with Fe as the dominating active metal, the ODH and DRB reactions are occurring with a ratio of 1:2–1:4 and the main product from the ODH of n -butane is 1,3-butadiene. The synergetic effect between Ni and Fe can improve the catalyst activity, stability and selectivity to ODH products. This finding is in accordance with our previous studies on the reaction of CO_2 and ethane [35]. The metal components (*i.e.*, Ni and Fe) are regarded to be responsible for the activation of n -butane, which can control the catalyst activity and tune the reaction pathways. Catalyst characterization results including XRD and in-situ XAFS show that the Ni species are in metallic state, while the Fe species are in the oxidized states.

DFT calculations were performed to shed light on the potential reaction pathways for the oxidative C–H (ODH) and C–C (DRB) bond cleavages of n -butane on $\text{Ni}(111)$ and $\text{FeO}/\text{Ni}(111)$ using the binding energies of the selected reaction intermediates (Table 3). The oxidative C–H bond cleavage of n -butane leads to the formation of $^*\text{CH}_2\text{CHCHCH}_2$, while the C–C bond cleavage of n -butane is investigated for the potential C–C bond scission of oxygenated $^*\text{CH}_3\text{CH}_2\text{CH}_2\text{CO}$ intermediate to form $^*\text{CH}_3\text{CH}_2\text{CH}_2 + ^*\text{CO}$. Fig. 10(a) shows that on $\text{Ni}(111)$, the initial step along the C–C bond cleavage pathway is slightly more favorable than the corresponding step along

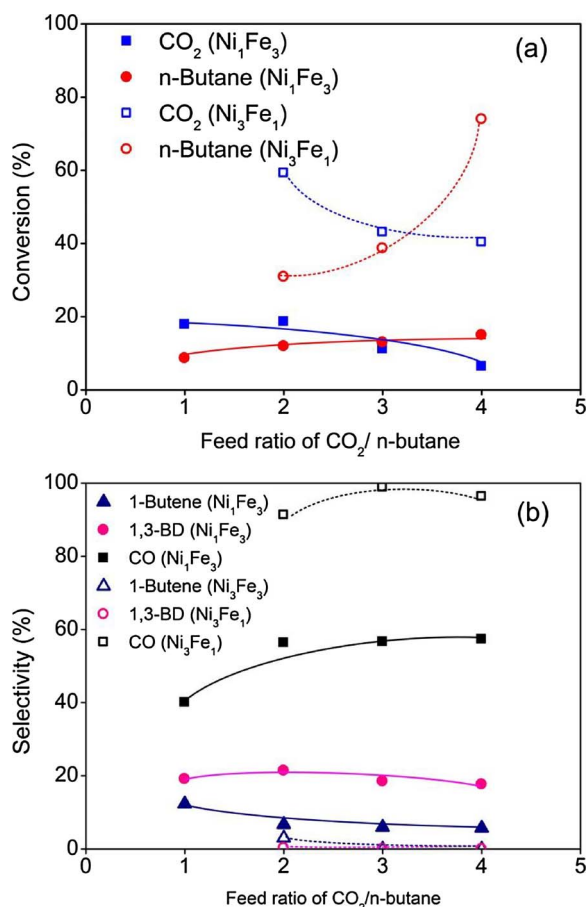


Fig. 8. Conversions of (a) CO₂ and *n*-butane, and (b) selectivities to 1-butene, 1,3-butadiene and DRB over Ni₁Fe₃/CeO₂ and Ni₃Fe₁/CeO₂ plotted versus inlet feed ratios CO₂/*n*-butane (CO₂/*n*-Butane/Ar = 1:1:18, 2:1:17, 3:1:16 or 4:1:15, 1 atm, 873 K).

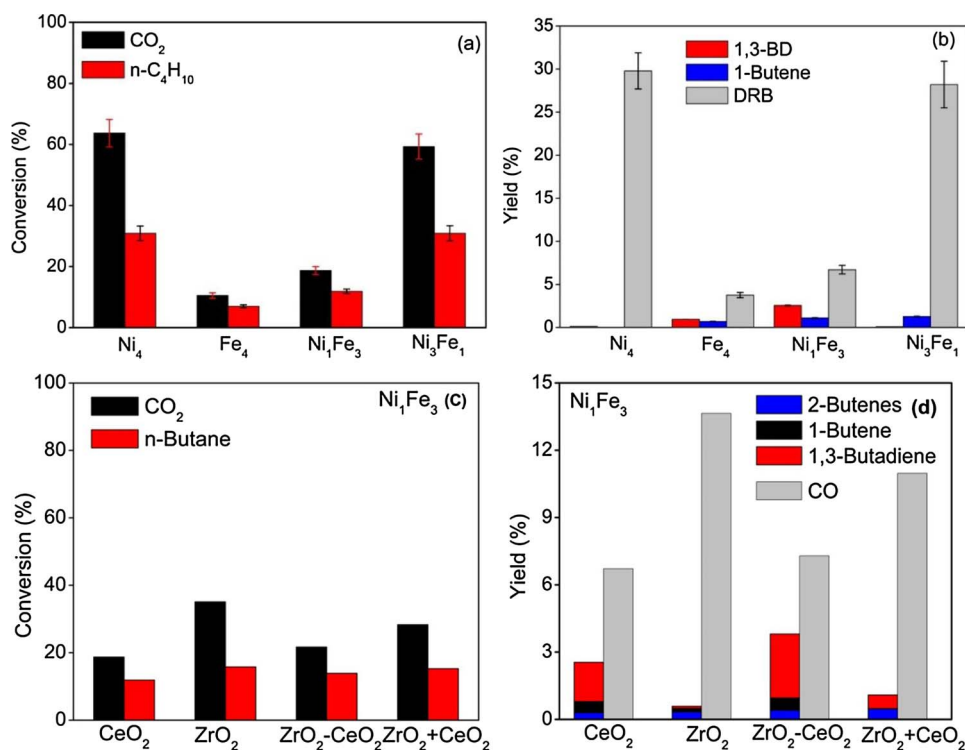


Fig. 9. Conversions of (a) CO₂ and *n*-butane, and (b) products distribution over CeO₂ supported catalysts; conversions of (c) CO₂ and *n*-butane, and (d) product distributions over Ni₁Fe₃ supported on different supports at the steady-state (CO₂/*n*-Butane/Ar = 2:1:17, 1 atm, 873 K).

Table 3

DFT calculated binding energies of potential intermediates for the C–H and C–C bond cleavage of *n*-butane.

Entry	Adsorbate	Binding Energy (eV)	
		Ni(111)	FeO/Ni(111)
1	CH ₃ CH ₂ CH ₂ CH ₂	−1.59	−1.40
2	CH ₃ CH ₂ CHCH ₂	−3.67	−3.47
3	CH ₃ CHCHCH ₂	−1.79	−1.64
4	CH ₂ CHCHCH ₂	−1.23	−1.11
5	CH ₃ CH ₂ CH ₂	−1.59	−0.96
6	CH ₃ CH ₂ CH ₂ CH ₂ O	−2.77	−2.89
7	CH ₃ CH ₂ CH ₂ CHO	−0.41	−0.94
8	CH ₃ CH ₂ CH ₂ CO	−2.20	−2.46
9	CO	−1.98	−2.04
10	O	−5.40	−5.78

the C–H bond cleavage pathway. This suggests that Ni(111) may promote the C–C bond scission of *n*-butane to produce syngas. In contrast, Fig. 10(b) shows that on FeO/Ni(111), the initial steps along the C–C and C–H bond scission are almost equal in energy, however, the subsequent two steps along the C–H bond cleavage pathway are energetically more favorable than those steps along the C–C bond cleavage pathway. Thus, FeO/Ni(111) is predicted to promote the C–H bond cleavage of *n*-butane leading to the formation of 1,3-butadiene.

In addition to the active metal species, another factor affecting the reaction pathways of *n*-butane with CO₂ is the oxide support, as indicated in Fig. 9(c) and (d). CeO₂ is a highly reducible oxide that can be easily reduced to Ce³⁺, and the reduced oxide has a strong tendency to react with CO₂, even causing the direct C–O bond scission [20,51]. For example, for the Ni₁Fe₃/CeO₂ catalyst, *n*-butane adsorbed on the supported metal species (*i.e.*, Ni and Fe) is dissociated *via* the cleavage of C–C and/or C–H bonds to form carbon and H species, which migrate to the metal-support interface to reduce the CeO₂ support and release the CO and H₂O products, while the lattice oxygen removed by the reaction with carbon or H species keeps being replenished by the gas-phase CO₂.

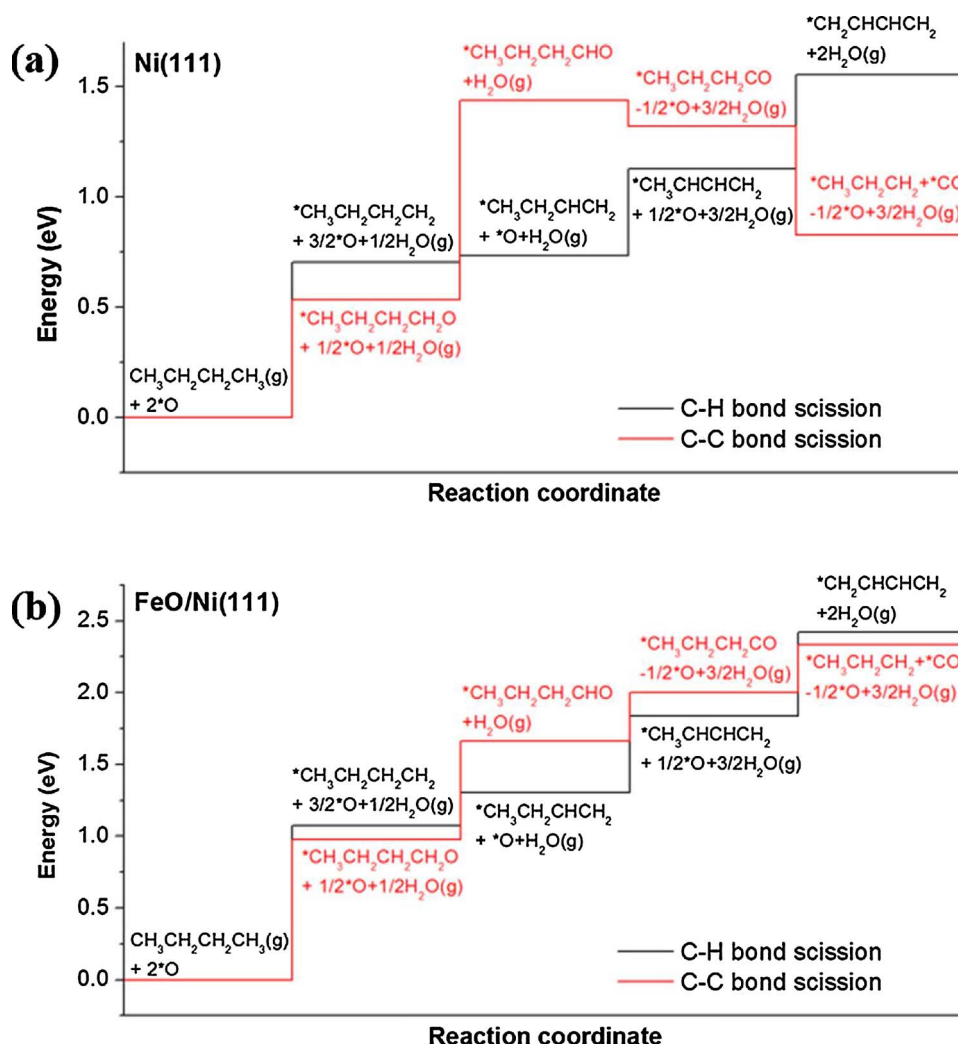


Fig. 10. DFT-calculated energy profile of DRB and ODH of *n*-butane on (a) Ni(111) and (b) FeO/Ni(111). * denotes adsorbed surface species.

The CeO_2 - ZrO_2 supported catalyst should adopt a similar mechanism. In addition, the enhanced oxygen storage capacity of the CeO_2 - ZrO_2 support should contribute to an improved catalyst activity and selectivity to the ODH pathway. In the case of ZrO_2 supported catalysts, the amount of reducible oxygen species in ZrO_2 is reported to be much less than that in either CeO_2 or CeO_2 - ZrO_2 , which might be responsible for the changes in both activity and selectivity. Further studies are required to obtain more mechanistic insights into the support effect.

5. Conclusions

The catalytic conversion of *n*-butane with CO_2 has been investigated over NiFe bimetallic catalysts. Both the ODH and DRB pathways combine the reduction of CO_2 and conversion of *n*-butane to useful chemical intermediates. Based on the results and discussion presented above, the following conclusions could be made: (1) In terms of activity and selectivity, $\text{Ni}_3\text{Fe}_1/\text{CeO}_2$ and Ni_4/CeO_2 primarily undergo the DRB pathway with a high activity to produce syngas, while $\text{Ni}_1\text{Fe}_3/\text{CeO}_2$ and Fe_4/CeO_2 show promising selectivity to the ODH of *n*-butane to 1,3-butadiene with a relatively low activity. (2) Catalyst characterizations demonstrate that the Ni active species are in the metallic state while Fe mainly exists as FeO_x . (3) DFT calculations further compare the ODH and DRB pathways over Ni(111) and FeOx/Ni(111) model surfaces, suggesting that Ni(111) favors the C–C bond scission while FeOx/Ni(111) may promote the C–H bond cleavage. (4) The support effect is observed due to the differences in reducibility and oxygen mobility of

supports that determine the activation of CO_2 , where CeO_2 and CeO_2 - ZrO_2 promote the ODH pathway and ZrO_2 only favors the DRB pathway.

Acknowledgements

This work is supported under Contract No. DE-SC0012704 with the U.S. Department of Energy, Division of Chemical Science. The in-situ XAFS spectra were collected at beamline 2-2 of the Stanford Synchrotron Radiation Lightsource (SSRL), with help from the Synchrotron Catalysis Consortium (Grant #DE-FG02-05ER15688). The DFT calculations were performed at the center for Functional Nanomaterial, a user facility at Brookhaven National Library which is sponsored by the U.S. DOE office of Science under Contract No. DE-AC02-05CH11231. T.F. Wang was supported by the National Natural Science Foundation of China (No. 21676155) and Program for New Century Excellent Talents in University of China (NCET-12-0297). X.D. Li was partially sponsored by the China Scholarship Council (CSC).

References

- [1] H.M. Torres Galvis, K.P. de Jong, ACS Catal. 3 (2013) 2130–2149.
- [2] J.J.H.B. Sattler, J. Ruiz-Martinez, E. Santillan-Jimenez, B.M. Weckhuysen, Chem. Rev. 114 (2014) 10613–10653.
- [3] B.R. Jermy, B.P. Ajayi, B.A. Abussaud, S. Asaoka, S. Al-Khattaf, J. Mol. Catal. A: Chem. 400 (2015) 121–131.
- [4] E.V. Makshina, M. Dusselier, W. Janssens, J. Degreve, P.A. Jacob, B.F. Sels, Chem.

- Soc. Rev. 43 (2014) 7917–7953.
- [5] W.C. White, *Chem. Biol. Interact.* 166 (2007) 10–14.
- [6] J. Rischard, C. Antinori, L. Maier, O. Deutschmann, *Appl. Catal. A: Gen.* 511 (2016) 23–30.
- [7] S.A. Bocanegra, S.R. de Miguel, I. Borbath, J.L. Margitfalvi, O.A. Scelza, *J. Mol. Catal. A: Chem.* 301 (2009) 52–60.
- [8] G. Tanimu, B.R. Jermy, S. Asaoka, S. Al-Khattaf, *J. Ind. Eng. Chem.* 45 (2017) 111–120.
- [9] I.C. Marcu, I. Sandulescu, J.M.M. Millet, *J. Mol. Catal. A: Chem.* 203 (2003) 241–250.
- [10] L.M. Madeira, M.F. Portela, *Catal. Rev.* 44 (2002) 247–286.
- [11] M.B. Ansari, S.E. Park, *Energy Environ. Sci.* 5 (2012) 9419–9437.
- [12] S. Wang, Z.H. Zhu, *Energy Fuel* 18 (2004) 1126–1139.
- [13] M.A. Atanga, F. Rezaei, A. Jawad, M. Fitch, A.A. Rownaghi, *Appl. Catal. B: Environ.* 220 (2018) 429–445.
- [14] J. Hansen, M. Sato, R. Ruedy, K. Lo, D.W. Lea, M. Medina-Elizade, *Proc. Natl. Acad. Sci.* 103 (2006) 14288–14293.
- [15] M.M. Bhasin, J.H. McCain, B.V. Vora, T. Imai, P.R. Pujadó, *Appl. Catal. A: Gen.* 211 (2001) 397–419.
- [16] V.R. Choudhary, K.C. Mondal, S.A.R. Mulla, *J. Chem. Sci.* 118 (2006) 261–267.
- [17] T. Osaki, T. Mori, *React. Kinet. Catal. Lett.* 89 (2006) 333–339.
- [18] C.N. Hamelinck, A.P.C. Faaij, H. den Uil, H. Boerrigter, *Energy* 29 (2004) 1743–1771.
- [19] Y.T. Shah, T.H. Gardner, *Catal. Rev.* 56 (2014) 476–536.
- [20] B. Yan, X. Yang, S. Yao, J. Wan, M. Myint, E. Gomez, Z. Xie, S. Kattel, W. Xu, J.G. Chen, *ACS Catal.* 6 (2016) 7283–7292.
- [21] N. Hotz, M.J. Stutz, S. Loher, W.J. Stark, D. Poulikakos, *Appl. Catal. B: Environ.* 73 (2007) 336–344.
- [22] G. Raju, B.M. Reddy, S.E. Park, *J. CO₂ Util.* 5 (2014) 41–46.
- [23] A. Löfberg, J. Guerrero-Caballero, T. Kane, A. Rubbens, L. Jalowiecki-Duhamel, *Appl. Catal. B: Environ.* 212 (2017) 159–174.
- [24] G. Raju, B.M. Reddy, B. Abhishek, Y.H. Mo, S.E. Park, *Appl. Catal. A: Gen.* 423 (2012) 168–175.
- [25] K. Nakagawa, C. Kajita, N.O. Ikenaga, M. Nishitani-Gamo, T. Ando, T. Suzuki, *Catal. Today* 84 (2003) 149–157.
- [26] F. Urian, I.C. Marcu, I. Sandulescu, *Catal. Commun.* 9 (2008) 2403–2406.
- [27] D. Fang, X. Zhang, M. Dong, X. Xue, J. Hazard. Mater. 336 (2017) 8–20.
- [28] V.D.B.C. Dasireddy, M. Hus, B. Likozar, *Catal. Sci. Technol.* 7 (2017) 3291–3302.
- [29] B. Su, Z.C. Cao, Z.J. Shi, *Acc. Chem. Res.* 48 (2015) 886–896.
- [30] J. Ashok, S. Kawi, *ACS Catal.* 4 (2014) 289–301.
- [31] S.M. Kim, P.M. Abdala, T. Margossian, D. Hosseini, L. Foppa, A. Armutlulu, W. van Beek, A. Comas-Vives, C. Copéret, C. Müller, *J. Am. Chem. Soc.* 139 (2017) 1937–1949.
- [32] M. Koike, D. Li, Y. Nakagawa, K. Tomishige, *ChemSusChem* 5 (2012) 2312–2314.
- [33] J.A. Rodriguez, P. Liu, D.J. Stacchiola, S.D. Senanayake, M.G. White, J.G. Chen, *ACS Catal.* 5 (2015) 6696–6706.
- [34] G. Nahar, V. Dupont, *Renew. Sust. Energy Rev.* 32 (2014) 777–796.
- [35] M. Myint, B. Yan, J. Wan, S. Zhao, J.G. Chen, *J. Catal.* 343 (2016) 168–177.
- [36] W.W. Loneragan, D.G. Vlachos, J.G. Chen, *J. Catal.* 271 (2010) 239–250.
- [37] P. Hohenberg, W. Kohn, *Phys. Rev.* 136 (1964) B864–B871.
- [38] P. Hohenberg, L.J. Sham, *Phys. Rev.* 140 (1965) A 1133.
- [39] G. Kresse, J. Furthmüller, *Comp. Mater. Sci.* 6 (1996) 15–50.
- [40] G. Kresse, J. Hafner, *Phys. Rev. B* 48 (1993) 13115–13118.
- [41] G. Kresse, D. Joubert, *Phys. Rev. B* 59 (1999) 1758–1775.
- [42] P.E. Blöchl, *Phys. Rev. B* 50 (1994) 17953–17979.
- [43] J.P. Perdew, Y. Wang, *Phys. Rev. B* 46 (1992) 12947–12954.
- [44] H.J. Monkhorst, J.D. Pack, *Phys. Rev. B* 13 (1976) 5188–5192.
- [45] H. Tan, J. Wang, S. Yu, K. Zhou, *Environ. Sci. Technol.* 49 (2015) 8675–8682.
- [46] S. Badoga, R.V. Sharma, A.K. Dalai, J. Adjaye, *Fuel* 128 (2014) 30–38.
- [47] B.M. Reddy, A. Khan, P. Lakshmanan, M. Aouine, S. Lorient, J.C. Volta, *J. Phys. Chem. B* 109 (2005) 3355–3363.
- [48] X. Du, D. Zhang, L. Shi, R. Gao, J. Zhang, *J. Phys. Chem. C* 116 (2012) 10009–10016.
- [49] F. Frusteri, S. Freni, V. Chiodo, S. Donato, G. Bonura, S. Cavallaro, *Int. J. Hydrogen Energy* 31 (2006) 2193–2199.
- [50] A.S. Reddy, C.Y. Chen, C.C. Chen, S.H. Chien, C.J. Lin, K.H. Lin, C.L. Chen, S.C. Chang, *J. Mol. Catal. A: Chem.* 318 (2010) 60–67.
- [51] M.D. Porosoff, B. Yan, J.G. Chen, *Energy Environ. Sci.* 9 (2016) 62–73.